^{1}H NMR Study of the Influence of Hemin Vinyl→Methyl Substitution on the Interaction between the *C*-Terminus and Substrate and the "Aging" of the Heme Oxygenase from *Neisseria meningitidis*: Induction of Active Site Structural Heterogeneity by a Two-Fold Symmetric Hemin†

Yangzhong Liu,‡ Li-Hua Ma,‡ Xuhong Zhang,§ Tadashi Yoshida,§ James D. Satterlee,|| and Gerd N. La Mar*,§

Department of Chemistry, University of California, Davis, California 95616, Department of Biochemistry, Yamagata University School of Medicine, Yamagata 990-9585, Japan, and Department of Chemistry, Washington State University, Pullman, Washington 99164

Received August 24, 2006

ABSTRACT: Solution ^{1}H NMR has been used to characterize the active site molecular and electronic structure of the cyanide-inhibited 2,4-dimethyldeuterohemin complex of the heme oxygenase from *Neisseria meningitidis* (*Nm*HO) with respect to the mode of interaction of the *C*-terminus with the substrate and the spontaneous "aging" of *Nm*HO that results in the cleavage of the *C*-terminal Arg208-His209 dipeptide. The structure of the portion involving residues Ala12-Phe192 is found to be essentially identical to that of the protohemin complex in either solution or crystal. However, His207 from the *C*-terminus is found to interact strongly with the substrate $1CH_3$, as opposed to the $8CH_3$ in the protohemin complex. The different mode of interaction of His207 with the alternate substrates is attributed to the 2-vinyl group of protohemin sterically interfering with the optimal orientation of the proximal helix Asp27 carboxylate that serves as acceptor to the strong H-bond by the peptide of His207. The 2,4-dimethyldeuterohemin HO complex "ages" in manner similary to that of protohemin, (Liu, Y., Ma, L.-H., Satterlee, J.D., Zhang, X., Yoshida, T., and La Mar, G. N., (2006) *Biochemistry 45*, 3875−3886) with mass spectrometry and *N*-terminal sequencing indicating that the Arg208-His209 dipeptide is cleaved. The 2,4-dimethyldeuterohemin complex of WT HO populates an equilibrium isomer stabilized in low phosphate concentration for which the axial His imidazole ring is rotated by ∼20° from that in the WT. The His ring reorientation is attributed to Asp24 serving as the H-bond acceptor to the His207 peptide NH, rather than to the His23 ring $N_\delta H$ as in the crystals. The functional implications of the altered *C*-terminal interaction with substrate modification are discussed.

Heme oxygenase, HO,[1] is a nonmetal enzyme that stereoselectively degrades protohemin, PH, into biliverdin, iron, and CO (*1*). The membrane-bound ∼300 residue mammalian HOs serve to degrade the toxic hemin into antioxidant biliverdin (*2*) (later to bilirubin via biliverdin reductase) in its key role in iron homeostasis (*3*) and CO as a putative neural messenger (*4*). Smaller, soluble plant and cyanobacterial HOs generate open tetrapyrroles as precursors (*5*) to light harvesting pigments and some pathogeneic bacteria, such as *Corynebacterium diphtheriae*, (*6*) *Cd*, *Neisseriae meningitidis*, (*7*) *Nm*, and *Pseudomonas aeruginosa*, (*8*) *Pa*, utilize ∼200 residue soluble HOs to "mine" (*9*−*12*) iron from the host. Although the diverse HOs exhibit variable degrees of sequence homology to mammalian HOs, (*11*) the structurally characterized HOs exhibit the same fold (*13*−*17*) and catalytic mechanism (*2*, *9*, *10*, *18*, *19*). The reaction proceeds via three distinct intermediates, meso-hydroxy-PH, verdoheme, and iron biliverdin (*2*, *9*, *10*), where the activated O_2 species is a ferric hydroperoxy species (*2*, *9*, *10*, *12*, *18*−*21*) rather than the more common ferryl species. The stereoselectivity of the heme cleavage has been shown to be controlled by two factors. The distal helix is placed so close to the heme surface so as to sterically block (*13*−*17*, *22*) all but one meso-position to attack by Fe^{III}-OOH, whereas steric interactions between the distal helix and the bound ligand (O_2, (*23*) but also NO, (*22*, *24*) CN^-, (*25*) N_3^- (*26*), and CO (*16*, *25*)) sterically tilt/orient the ligand toward the lone "unblocked" meso position. Although the majority of HOs are exclusively α-stereoselective (*2*, *9*, *10*), *Pa*HO exhibits mixed *β*,*δ*-stereoselectivity (*27*). The different stereoselectivity of *Pa*HO relative to that of other HOs has been shown to result from a seating of the PH in the active

† This work was supported, in part, by the National Institutes of Health Grants GM62830 (to G.N.L.) and GM47645 (to J.D.S.) and a Grant-in-Aid for Scientific Research (16570102) from the Ministry of Education and Sports, Science and Teaching, Japan (to T.Y.).

* Corresponding author. Phone: (530) 752-0958. Fax: (530) 752-8995. E-mail: lamar@chem.davis.edu.

‡ University of California, Davis.

§ Yamagata University School of Medicine.

|| Washington State University.

[1] Abbreviations: DSS, 2,2-dimethyl-2-silapentane-5-sulfonate; DMDH, 2-, 4-dimethyldeuterohemin; PH, protohemin, NOESY, two-dimensional nuclear Overhauser spectroscopy; TOCSY, two-dimensional total correlation spectroscopy; HO, heme oxygenase; *Nm*HO, *Neisseria meningitidis*; *Nm*HO-DMDH-CN, *Neisseria meningitidis* heme oxygenase-2-,4-dimethyldeuterohemin-cyanide; *Nm*HO-PH-CN, *Neisseria meningitidis* heme oxygenase-protohemin-cyanide; MALDI-TOF, matrix-assisted laser desorption ionization -time-of-flight.

10.1021/bi061747q CCC: $33.50
Published on Web 10/26/2006

site that is rotated 90° about the heme normal relative to that in other HOs (*17*, *27*). The variable β- versus δ-stereoselectivity for *Pa*HO arises because of the ubiquitous heme orientational heterogeneity about the PH α-,γ-meso axis; (*28*−*31*) for α-stereoselectivity HOs, this isomerism has no consequence.

The unusual hydroperoxy species (*2*, *9*, *10*, *12*, *19*) as the activated complex that initiates the reaction is unique to HOs, and the inhibition of the O−O bond cleavage common (*18*, *32*) to cytochromes P450 and heme peroxidases and the stabilization of the Fe-OOH unit appear to be mediated by a series of distal ordered water molecules (*17*, *22*−*24*, *26*) that are organized in a channel by a H-bond network with some unusually strong H-bonds (*30*, *31*, *33*−*35*). The distal interaction with water molecules embedded in the H-bond network is observed in each of the structurally characterized HOs, in spite of only limited sequence homology for the members of the H-bond network. Although the molecular structure and mechanism of the diverse HOs have been shown to be remarkably similar, less attention has been paid to the particularly distinctive properties of the individual HOs. Even the unique stereoselectivity in *Pa*HO is rationalized by a conserved fold and mechanism, with only the heme seating altered (*17*, *27*).

HOs initially bind PH 1:1 disordered about the α-,γ-meso-axis, with the relative populations changing with time and/or ligand until a new equilibrium ratio is attained (*28*−*31*). In most cases, both heme orientations remain populated to a significant degree at equilbrium (*28*−*30*). For solution NMR investigations, this equilibrium heme orientational heterogeneity introduces severe spectral resolution and sensitivity problems for most HOs that have been obviated by the use of the synthetic, 2-fold symmetric substrate, 2,4-dimethyldeuterohemin (DMDH, R═CH_3 in Figure 1) (*30*, *33*). *Nm*HO and *Pa*HO exhibit less sequence homology (*11*) to mammalian HOs than does *Cd*HO and exhibit more compact structures (*15*, *17*, *22*) with fewer and/or smaller vacancies near the distal pocket than mammalian HOs (*13*, *24*−*26*) or *Cd*HOs (*16*, *23*). The more "restrictive" heme pocket in *Nm*HO is further confirmed by the equilibrium population of primarily a single PH orientation, (*31*, *36*) and by increased dynamic stability in the pocket relative to that of other HOs as reflected in labile proton exchange with solvent (*31*).

The crystal structure of *Nm*HO complexes showed that the *C*-terminus is closer to the heme pocket than that in other HOs, but the penultimate His207Arg208His209 fragment could not be detected and was proposed to be statically or dynamically disordered (*15*, *22*). Moreover, the conversion from a H-bond donor ligand (*Nm*HO-PH-H_2O) to a H-bond acceptor (*Nm*-PH-NO) resulted in a major reorientation of the 7-propionate as well as several other distal pocket residues (*15*, *22*). Solution ^{1}H NMR, however, located (*31*, *37*) one of the *C*-terminal His in the heme pocket interacting with pyrrole D ($8CH_3$). The proposed His207 peptide NH was inserted into the heme pocket and serves as a likely H-bond donor to the Asp27 carboxylate, whereas the Arg208 guanidyl group was proposed to orient toward the distal pocket and form a salt bridge with the reoriented 7-propionate (*31*, *37*).

We extend herein our investigation to some unusual properties of the *Nm*HO relative to those of other HOs.

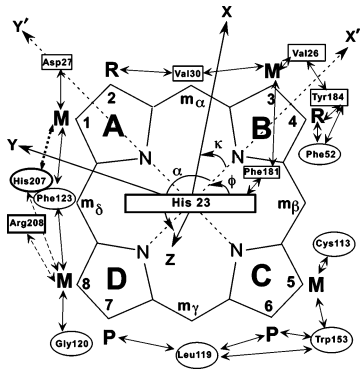

FIGURE 1: Schematic structure of the heme pocket showing the disposition of proximal (rectangles) and distal (ovals) residues relative to each other and the heme, as viewed from the proximal side. R_2═R_4 = vinyl corresponds to native protohemin (PH), whereas R_2═R_4 = methyl corresponds to the 2-fold symmetric 2,4-dimethyldeuterohemin (DMDH). The Fischer notation identifies the substrate substituents for both PH and DMDH. The NOESY contacts, expected on the basis of the crystal structure, (*22*) and observed in solution, are shown as double-sided solid arrows. Two observed NOESY contacts for the PH complex not predicted by the crystal structure involving His207 and Arg208 (shown in bold), but observed in solution, (*31*, *37*) are shown by dashed lines for the PH complex and by dotted lines in the 2,4-dimethyldeuterohemin (DMDH) complex. Also shown are the references *x*′, *y*′, and *z*′ and the magnetic *x*, *y*, and *z* coordinate systems, where *z*′ is normal to the heme. The angle β defines the tilt of the major magnetic axis *z* from the heme normal *z*′ (not shown) and the angle α between the projection of *z* on the *x*′, *y*′ plane, and the *x*′ axis defines the direction of tilt, and $\kappa \sim \alpha + \gamma$ locates the rhombic or *x*, *y* axes relative to the *x*′, *y*′ axes.

However, although the unsymmetric PH leads to one dominant orientation at equilibrium in *Nm*HO-PH-CN, (*31*) *Nm*HO-PH-H_2O, (*36*) and *Nm*HO-PH-N_3 (*38*) complexes, the replacement of PH with the 2-fold symmetric DMDH (Figure 1, R = CH_3) leads to the equilibrium population of two interconverting species whose relative stabilities are modulated by solution conditions and whose heme methyl hyperfine shift pattern reflects a significant difference in the rotational position of the prosthetic group relative to the axial His imidazole plane. Also, we observe that the replacement of PH by DMDH significantly alters the interaction between the substrate and the *C*-terminus. The replacement of PH with DMDH for cyanide complexes of hHO (*29*, *33*) and *Cd*HO (*30*) leads to very small changes in the pattern of dipolar shifts for the proximal helix residues in particular. In contrast, significant changes in the proximal helix hyperfine shift in the *Nm*HO complex indicate systematic changes in either the molecular or the electronic structure. We emphasize herein a comparison of the mode of *C*-terminal interaction of the *C*-terminus with the substrate when the PH vinyls are replaced by methyls and the development of a hypothesis for the induction of structural heterogeneity in the substrate binding for this vinyl → methyl substitution. Finally, we have shown that the native *Nm*HO, (*37*) which consists of Ser2-His209, undergoes a spontaneous, irreversible conversion to a new species with a detectably different ^{1}H NMR spectrum for the PH cyanide complex. Although the actual cleavage of the Arg208His209 dipeptide from WT *Nm*HO is not likely physiologically relevant, the fact that the cleavage results (*37*) in significantly altered biliverdin release and exogenous ligation rates argues for a physiological role for the interaction of the *C*-terminus with the

substrate that modulates product release. Our interest here is to find out if, and how, the *C*-terminal peptide is influenced by substrate substituents.

MATERIALS AND METHODS

Protein Preparation. Apo *Nm*HO samples utilized in this study are the same as those described in detail previously (*31*). All samples were kept frozen at −80 °C until required. A stoichiometric amount of 2,4-dimethyldeuterohemin, DMDH, was added to apo *Nm*HO in phosphate buffer (100 mM or 50 mM at pH 7.0). The substrate complex was purified by column chromatography on Sephadex G25 and concentrated to 2−3 mM by ultrafiltration. KCN buffered at pH 7.0 was added in ∼10-fold molar excess to prepare the cyanide complex, *Nm*HO-DMDH-CN. ^2H_2O for ^1H_2O solvent exchange was carried out by column chromatography (*39*).

Samples of *Nm*HO-DMDH-H_2O and *Nm*HO−DMDH-CN were aged (*37*) at 25 °C for 5−25 h; the longer times comparable to the duration of the acquisition of the minimal 2D NMR data sets required for structural elucidation. The aging was monitored by mass spectrometry and ^{1}H NMR as the *Nm*HO-DMDH-CN complex.

NMR Spectroscopy. ^{1}H NMR data were collected on Bruker AVANCE 500 and 600 spectrometers operating at 500 and 600 MHz, respectively. Reference spectra were collected in ^1H_2O over the temperature range 15−35 °C at a repetition rate of 1 s^{-1} using a standard one-pulse sequence. Chemical shifts are referenced to 2,2-dimethyl-2-silapentane-5-sulfonate (DSS) through the water resonance calibrated at each temperature. The 600 MHz NOESY (*40*) spectra (mixing time, 40 ms; 15−35 °C) and 500 MHz Clean-TOCSY (to suppress the ROESY response (*41*)) spectra (25° and 35 °C, spin lock 25 and 40 ms) using MLEV-17 (*42*) were recorded over a bandwidth of 25 kHz (NOESY) and 12 kHz (TOCSY) with recycle times of 500 ms and 1s, using 512 t1 blocks of 128 and 256 scans each consisting of 2048 t2 points. 2D data sets were processed using Bruker XWIN software on a Silicon Graphics Indigo workstation and consisted of 30°- or 45°-sine-squared-bell-apodization in both dimensions and zero-filled to 2048 × 2048 data points prior to Fourier transformation.

Mass Spectrometry. Matrix assisted laser desorption ionization-time-of-flight (MALDI-TOF) mass spectrometry was carried out on a Voyager DE system (Perseptive Biosystems) housed in the Washington State University Laboratory for Biotechnology and Bioanalysis, Unit 2 (WSU LBB2). Five primary matrix solutions were employed in replicates of each *Nm*HO sample. These were made from saturated solutions of sinapinic Acid (3,5-dimethoxy-4-hydroxy-cinnamic acid, Aldrich or Sigma). The aqueous solutions used to dissolve the matrix were (i) 30%−0.1% trifluoroacetic acid/70% acetonitrile (Sigma) by volume; (ii) 30%−1.0% trifluoroacetic acid/70% acetonitrile; (iii) 50%−1.0% trifluoroacetic acid/50% acetonitrile; (iv) 30%−1.0% acetic acid/70% acetonitrile; and (v) 50%−1.0% acetic acid/50% acetonitrile. Protein samples (1 mL) were thoroughly pipet-mixed with an equal volume of the matrix solution on the MALDI-TOF plate until crystallization began. For calibration purposes, standard desalted solutions of (all from Sigma) equine myoglobin (M_r = 16,952.56) and equine cytochrome *c* (M_r = 12,361.14) were incorporated in some solutions as internal standards for accurate mass/charge determinations. Mass statistics were accumulated using repeated mass determinations in separate MALDI-TOF experiments with at least two internal references present. Individual protein masses were calculated using the averaged isotope masses of each element (IUPAC Commission on Atomic Weights and Isotopic Abundances, 1993): H = 1.00794, C = 12.011, N = 14.00674, O = 15.9994, S = 32.066. Protein masses were then constructed from the calculated mass of each amino acid and the specific primary amino acid sequence.

N-Terminal Sequencing. Amino-terminal protein sequencing (up to 12 amino acids) was carried out at the Washington State University Laboratory for Biotechnology and Bioanalysis, Unit 1 (WSU LBB1) using an Applied Biosystems Procise 492 Protein Sequencer.

HPLC Analysis of the NmHO DMDH-Reaction Products. The reaction mixture consists of 20 μM *Nm*HO-DMDH complex and 1 mM desferrioxamine in 1.0 mL of 50 mM phosphate (pH 7.4). After 3 min of preincubation, the reaction was started by the addition of 10 μL of 1 M sodium ascorbate (final 10 mM) for 2 h, followed by hydrolysis with HCl to ensure the full conversion into dimethyl-α-deuterobiliverdin. Stereoselectivity of the reaction products was analyzed by HPLC according to the method used for the analysis of the reaction products from PH (*43*).

Magnetic Axes Determination. The location of the magnetic axes in *Nm*HO-DMDH-CN were determined by finding the Euler rotation angles, Γ(α,*β*,*γ*), that rotate the crystal-structure-based, iron-centered reference coordinate system *x*′, *y*′, *z*′ into the magnetic coordinate system *x*, *y*, *z*, where the paramagnetic susceptibility tensor, *χ*, is diagonal where α, *β*, *γ* are the three Euler angles (*31*, *44*−*46*). The angle dictates the tilt of the major magnetic axis, *z*, from the heme normal *z*′; α reflects the direction of this tilt and is defined as the angle between the projection of the *z*-axis on the heme plane and the *x*′ axis (Figure 1), and $\kappa \sim \alpha+\gamma$ is the angle between the projection of the *x*, *y* axes onto the heme plane and locates the rhombic axes (Figure 1). The magnetic axes are determined by a least-square search for the minimum in the error function: (*31*, *44*−*46*)

$$F/n = \sum_{i=1}^{n} |\delta_{dip}(obs) - \delta_{dip}(calc)|^2 \quad (1)$$

where the calculated dipolar shift in the reference coordinate system, *x*′, *y*′, *z*′, (*R*, *θ*′ Ω′), is given by

$$\delta_{dip}(calc) = (24\pi\mu_0 N_A)^{-1}[2\Delta\chi_{ax}(3\cos^2\theta' - 1)R^{-3} + 3\chi_{rh}(\sin^2\theta'\cos 2\Omega')R^{-3}]\Gamma(\alpha, \beta, \gamma), \quad (2)$$

with $\Delta\chi_{ax}$ and χ_{rh} as the axial and rhombic anisotropies of the diagonal paramagnetic susceptibility tensor. The observed dipolar shift, δ_{dip}(obs), is given by

$$\delta_{dip}(obs) = \delta_{DSS}(obs) - \delta_{DSS}(dia) \quad (3)$$

where δ_{DSS}(obs) and δ_{DSS}(dia) are the chemical shifts in ppm, referenced to DSS, for the paramagnetic *Nm*HO-DMDH-CN complex and an isostructural diamagnetic complex, respectively. In the absence of an experimental δ_{DSS}(dia), it

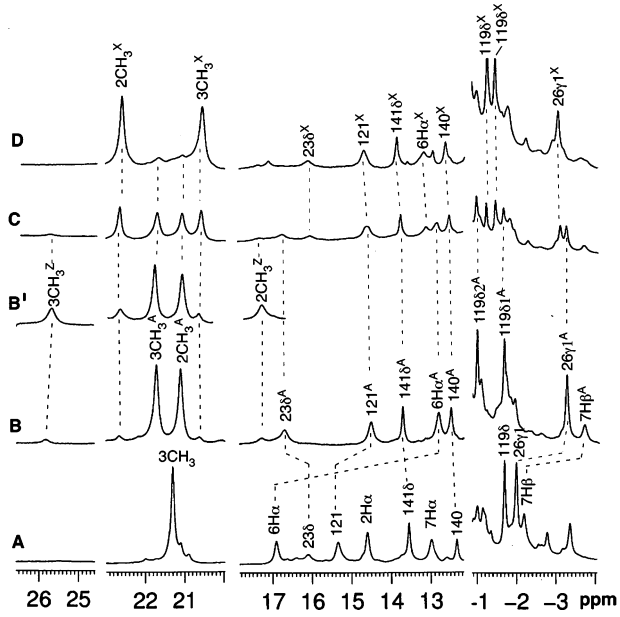

FIGURE 2: Resolved portions of the 600 MHz ^{1}H NMR spectrum of (A) *Nm*HO^A-PH-CN with reported (*31*) assignments; (B) *Nm*HO^A-DMDH-CN; (C) a sample composed of ~50% *Nm*HO^A-DMDH-CN and ~50% *Nm*HO^X-DMDH-CN; and (D) >95% *Nm*HO-DMDH^X-CN in ^1H_2O 100 mM, in phosphate at pH 7.0 at 25 °C. The inset B′ shows the relative intensities of the resolved heme methyl peaks in a 8:1 A/X *Nm*HO-DMDH-CN sample in 50 mM phosphate at pH 7.0 at 25 °C. Heme resonances are labeled by the Fischer notation and residue protons by their number and position. Although there is no unique labeling of DMDH in the Fischer notation, we label positions 1−8 on the basis of the position occupied by the corresponding subsituent in PH. Superscript A represents the peaks for the native, initially formed complex of Ser2-His209 *Nm*HO, superscript X identifies the analogous signals for complex X where Arg208 and His209 have been cleaved, and superscript Z identifies the peaks for a species in dynamic equilibrium with species A, for which the position of the equilibrium is strongly modulated by phosphate concentrations.

may be reasonably estimated (*31*, *47*, *48*) using the ShiftX program (*48*) and the available molecular structure (*22*).

RESULTS

Structural Heterogeneities of NmHO-DMDH-CN. The resolved portions of the 600 MHz ^{1}H NMR spectra of *Nm*HO^A-PH-CN and *Nm*HO^A-DMDH-CN are compared in Figure 2A and B, respectively, where *Nm*HO^A represents the native Ser2-His209 polypeptide (*37*). Heme resonances are labeled in the Fischer notation (Figure 1) and for residues, by the residue number and position (except peptide NHs, which are labeled only by residue number). Resonances from the alternate 'A' and 'X' forms are labeled by such superscripts. As is apparent in the comparison of Figure 2A and B, the chemical shifts for both heme substituents and amino acid residues differ significantly for the two substrates. A closer inspection of the spectrum (Figure 2B) for the *Nm*HO-DMDH-CN complex in 100 mM phosphate reveals two additional resolved (though broad) methyl peaks (labeled 3CH$_3^Z$ and 2CH$_3^Z$, respectively), which represent an ~10% (A/Z ~10:1) population of an equilibrium (see below) isomer of *Nm*HO^A-DMDH-CN, which we label species Z, or *Nm*HO^Z-DMDH-CN. When the phosphate concentration is reduced to 50 mM, the intensities of CH$_3^Z$ peaks increase relative to those of CH$_3^A$ to a new A/Z ratio 2:1 (inset B′ in Figure 2).

When ^{1}H NMR data are recorded at ~25 °C over a period of days as the cyanide complex (or over only several hours as the aquo complex), the peaks for the ^{1}H NMR spectrum of *Nm*HO^A-DMDH-CN decrease in intensity (compare Figure 2B with 2C), and a completely new species, labeled *Nm*HO^X-DMDH-CN, with new methyl peaks CH$_3^X$ emerges, as shown in Figure 2D. It will be shown that species X is the same as that obtained by "aging" the PH complex, namely, *Nm*HO^A with the *C*-terminal Arg208-His209 cleaved (*37*).

Figure 2 shows that the 'A' and 'X' complexes exhibit comparably narrow lines that are similar to those of the analogous PH complexes (*31*, *37*). Species Z exhibits inherently broader lines due to the exchange with species A and the lower concentration of Z, which make the detection of 2D cross peaks for this species much more difficult. Hence, we pursue 2D NMR assignments and structural characterization for the A and X complexes in great detail comparable to that reported previously for the analogous PH complexes (*31*, *37*). Only 2D data relevant to differences between the DMDH and PH complexes or between the 'A', 'X' and 'Z' complexes of DMDH are illustrated in the text; other relevant 2D data are provided in Supporting Information. Although DMDH does not possess a unique numbering system for its substituents, we adopt the labeling 1−8 for pyrrole positions and α−δ for the meso positions, on the basis of the location of the same numbered substituents for PH in the crystal (*15*, *22*) or solution structures (*31*, *37*) (i.e., 2CH$_3$ in DMDH refers to the methyl occupying the 2-vinyl position of PH in the protein matrix).

Mass Spectrometric Characterization of NmHO^X-DMDH-CN. The mass spectrum of the substrate complex is identical to that for apo-*Nm*HO, dictating that both the axial ligand and substrate are lost during ionization, as observed previously for the PH complex (*37*). The MALDI-TOF mass spectra of essentially pure *Nm*HO^A-DMDH-CN and a series of mixtures with increasing conversion to *Nm*HO^X-DMDH-CN (not shown; see Supporting Information) show that the 'A' species exhibits the same mass, M_r = 23,455 ± 13 Da (GenBank[2] accession number AAF24745 minus the first 21 residues, i.e., Ser2−209) (*31*), reported for pure *Nm*HO^A-PH-CN (*37*). Confirmation by *N*-terminal sequencing establishes that *Nm*HO^A-DMDH-CN possesses the same Ser2-His209 polypeptide as in the 'A' complex with PH. Similarly, *Nm*HO^X-DMDH-CN, with M_r = 23,166 ± 6 Da, exhibits a mass that is indistinguishable from that observed for *Nm*HO^X-PH-CN, M_r = 23,166 ± 13 Da (*37*), which, with the retained Ser2 as the initial residue by sequencing, dictates that the DMDH 'X' species consists of only residues Ser2-His207, with the Arg208-His209 cleaved in the 'A' → 'X' conversion. The rate of the 'A' → 'X' conversion under the same conditions is a factor ~5 times faster for DMDH than that for PH as both the aquo and cyanide complexes, (*37*) with the rate being much faster for H_2O than that for CN^- as ligand.

Resonance Assignments and Structural Characterization of NmHO^A-DMDH-CN. The DMDH resonances are assigned on the basis of the observation of characteristic strong and

[2] Protein Identification Resource, National Biomedical Research Foundation, Georgetown University Medical Center, Washington, D.C. 20007.

Table 1: Substrate Chemical Shifts for *Nm*HO-DMDH-CN and *Nm*HO-PH-CN Complexes[a]

	*Nm*HO^i-DMDH-CN			*Nm*HO^i-PH-CN[b]	
position	i = A[c]	i = X[d]	i = Z[e]	i = A	i = X
$1CH_3$	11.25	11.30	7.82	7.90	7.55
$2CH_3$	21.15	22.65	17.24		
$2H_\alpha$				14.48	14.79
$2H_\beta$s				−5.58, −6.62	−5.77, −6.79
$3CH_3$	21.67	20.50	25.60	21.40	21.00
$4CH_3$	9.07	8.12	12.48		
$4H_\alpha$				8.06	7.96
$4H_\beta$s				−3.38, −2.80	−3.09, −2.55
$5CH_3$	9.32	10.92		9.62	10.25
$6H_\alpha$s	5.74, 12.77	6.10, 13.03		1.14, 16.92	1.26, 16.40
$6H_\beta$s	−1.73, 0.35	−1.54, 0.45		−3.38, −1.02	−3.27, −0.88
$7H_\alpha$s	10.71, 7.81	10.41, 7.61		13.06, 5.33	12.62, 5.92
$7H_\beta$s	−3.72, −1.96	−2.97, −1.79		−2.17, −1.10	−2.01, −1.23
$8CH_3$	7.71	8.00		10.33	10.77
α-meso-H	−1.03	−2.18	−2.20	−2.21	−2.15
γ-meso-H	−1.64	−2.04		−1.72	−1.64

[a] Chemical shift in ppm, referenced to DSS via the solvent signal in ^1H_2O at pH 7.0 at 25 °C. [b] In ppm, referenced to DSS, in ^1H_2O, 100 mM phosphate at pH 7.0 at 25 °C, as reported in ref 31 (*31*). [c] The dominant complex, 100 mM phosphate, consisting of Ser2-His209 (*37*). [d] The "aged" complex, 100 mM phosphate, consisting of Ser2-His207 (*37*). [e] The equilibrium isomeric form of Ser2-His209 stabilized at low phosphate concentration.

weak NOESY cross peaks between substituents on the same and adjacent pyrroles (*33*, *46*), respectively (data not shown; see Supporting Information). The assignments were greatly facilitated by the resolution of one $C_\alpha H$ from each propionate and three of the four propionate C_βHs. The chemical shifts for DMDH in *Nm*HO^A-DMDH-CN are provided in Table 1, where they can be compared to those of *Nm*HO^A-PH-CN (*31*).

TOCSY and NOESY spectra (not shown; see Supporting Information) provided sequence-specific assignments for five extended helical fragments by the standard N_i-N_{i+1}, α_i-N_{i+1}, β_i-N_{i+1}, α_i-N_{i+3} and/or α_i-β_{i+3} dipolar connectivities (*49*) in the same manner as that reported in detail (*31*, *37*) for the PH complex, yielding the proximal helix sequence Ala17-Val26 with Val26 exhibiting its predicted pattern of NOESY cross peaks to $3CH_3$. In contrast to the PH complex, where Asp27 could not be assigned (*31*) because its cross peaks were lost in the very intense aliphatic envelope, this residue is assigned by TOCSY (see Supporting Information), and the expected NOESY cross peaks to the $1CH_3$ and Val26 are observed, as shown in Figure 3. Less complete, but sufficient, backbone connectivities locate Cys113-Leu119, with Cys113$C_\alpha H$ exhibiting the expected intense cross peak to $5CH_3$ and the methyls of Leu119 exhibiting NOESY cross peaks to the two propionates similar to those for the PH complex (*31*). The distinctive low-field shift and strong relaxivitiy confirm Ala121, but neither the relaxed Gly120 nor Ala122 NHs were resolved (as should have been expected; see below). The fragment Phe123-Phe125 was identified by sequential NOESY cross peaks, with the Phe123 backbone and ring exhibiting the expected cross peak to $1CH_3$. The loop, His137-Leu142, which contains two of the strongest H-bonds, was assigned by backbone connectivities that are the same as those reported for the PH complex (*31*). A fourth helical fragment consists of Ala180-Val187 and exhibits the same contacts as those in the PH complex. We consider these sequence-specific assignments robust. The chemical shifts for strongly dipolar-shifted ($\delta_{dip} \geq |1.0|$ ppm) proximal helix residues are listed in Table 2, and the remainder of the shift data are provided in Supporting Information.

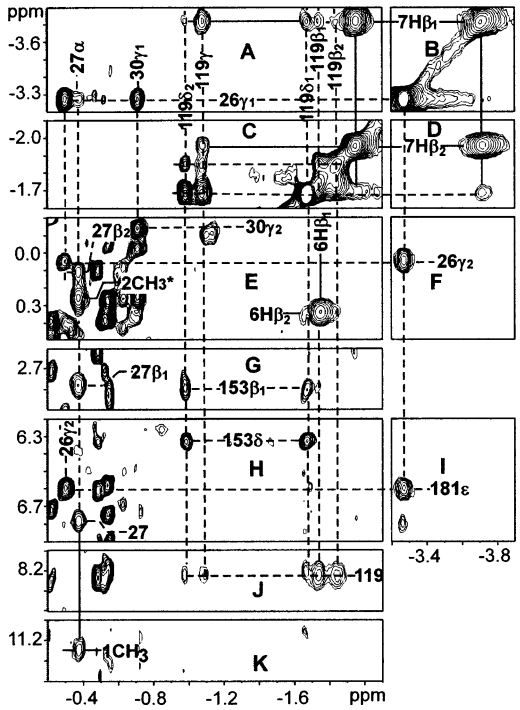

FIGURE 3: Upfield portion of the NOESY spectrum (mixing time 40 ms; repetition rate of 1 s^{-1}) of *Nm*HO^A-DMDH-CN in ^1H_2O 100 mM in phosphate at pH 7.0 at 25 °C, illustrating the intraresidue contact between Leu119 and propionate C_βHs (A, C), among Leu119 protons (C, J), among propionate C_βHs (A, B, D), between Leu119 and Trp153 (G, H), between Val26 and Phe181 (I), with Asp27 protons (E, G, H), and between Asp27 and both Val26 (A) and 1- CH_3 (K). The asterisk for $2CH_3$* indicates that the peak is folded in.

With the strong conservation of both NOESY contacts and the pattern of dipolar shifts for the sequentially assigned residues, another 20 residues could be assigned on the basis of the characteristic NOESY contacts among distinctive spin systems, as reported for the PH complex (*31*) and as predicted by the crystal structure (*22*). These assignments are reported only if a residue exhibits characteristic dipolar contacts to at least two other assigned residues. This "web" of contacts, together with the confirmation of the predicted

Table 2: Chemical Shifts for Strongly Hyperfine-Shifted Residues in *Nm*HO-DMDH-CN and *Nm*HO-PH-CN Complexes[a]

		δ_{DSS}(Obs)[a]				$\Delta\delta_{dip}$(calc)[b]
		*Nm*HO^i-DMDH-CN			*Nm*HO^i-PH-CN[c]	
residue	proton	i = A[d]	i = X[e]	i = Z[f]	i = A	
Thr19	NH	8.16	8.27		8.04	0.17
	CH	5.55	5.52		5.52	0.05
	$C_\beta H$	5.83	5.80		5.75	0.08
	$O_\gamma H$	6.21	6.00		5.90	0.26
	$C_\gamma H_3$	1.72	1.75		1.70	0.08
Thr20	NH	8.52	8.61		8.37	0.18
	CH	6.52	6.68	6.28	6.30	0.33
	CH	5.30	5.32	5.19	5.14	0.15
	$C_\gamma H_3$	2.45	2.42	2.39	2.27	0.2
Ala21	NH	9.41	9.38		9.36	0.05
	$C_\alpha H$	5.23	5.30		5.31	−0.03
	$C_\beta H_3$	1.96	2.00		2.04	−0.02
His23	NH	10.87	10.98		11.08	−0.19
	CH	6.12	6.13	7.22	7.37	−1.2
	$C_{\beta1}H$	11.45	11.30	11.87	11.56	
	$C_{\beta2}H$	10.33	10.57	9.40	10.75	
Asp24	NH	11.29	11.26		11.41	−0.27
	CH	6.37	6.42		6.80	−0.45
	$C_{\beta1}H$	3.43	3.60		3.65	−0.13
	$C_{\beta2}H$	4.14	4.17		4.30	−0.14
Val26	NH	7.56	7.61		8.33	−0.68
	CH	2.26	2.31	2.96	2.80	−0.48
	CH	0.06	0.23	1.89	1.60	−1.56
	$C_{\gamma1}H_3$	−3.28	−3.08	−1.91	−1.96	−0.98
	$C_{\gamma2}H_3$	−0.30	−0.17	0.75	0.51	−0.67
Asp27	$C_\alpha H$	−0.40	−0.33			−0.15
	$C_{\beta1}H$	2.77	2.55			−0.34
	$C_{\beta2}H$	0.25	0.35			−0.70

[a] Chemical shifts in ppm, referenced to DSS via the solvent peak, in ^1H_2O at pH 7.0 at 25 °C. [b] Difference in calculated dipolar shift, $\Delta\delta_{dip}(calc) = \delta_{dip}(calc:NmHO^A\text{-DMDH-CN}) - \delta_{dip}(calc:NmHO^A\text{-PH-CN})$, on the basis of magnetic axes ($\alpha = 200°$, $\beta = 8$, $\kappa = 40°$) for *Nm*HO^A-PH-CN and ($\alpha = 215$, $\beta = 12°$, $\kappa = 40°$) for *Nm*HO^A-DMDH-CN (see Supporting Information), using the conserved $\Delta\chi_{ax} = 2.48\ 10^{-8}$ m^3/mol and $\Delta\chi_{rh} = -0.58 \times 10^{-8}$ m^3/mol (*31*, *60*). [c] In ppm, referenced to DSS, in ^1H_2O, 100 mM phosphate at pH 7.0 at 25 °C, as reported in ref 31 (*31*). [d] The dominant complex in 100 mM phosphate concentration, consisting of the native Ser2-His209 polypeptide. [e] The "aged" complex, 100 mM phosphate, consisting of the Ser2-His207 polypeptide. [f] The equilibrium isomeric form of the Ser2-His209 polypeptide stabilized at low phosphate concentration.

pattern of dipolar shifts, makes even these assignments robust. The pattern of completely conserved intraresidue NOESY cross peaks encompasses the residues Phe11-Phe192. The 180° $\gamma-\delta$ bond rotated Gln49 and and 180° $\beta-\gamma$ His53, relative to those in the crystal structures (*15*, *22*), are confirmed by the NOESY cross peaks of the former residue $N_\epsilon H_2$ terminus to His141 (not shown) and the latter residue ring $N_\epsilon H$ to Phe52 (not shown), and Gln49, as reported for the solution structure of *Nm*HO-PH-CN (*31*), *Nm*HO-PH-H_2O (*36*), and *Nm*HO-PH-ON (*50*).

All observed NOESY cross peaks to DMDH could be interpreted on the basis of the predictions of the crystal structure (*22*) with methyls replacing vinyls, with one very major exception. The crystal structure predicts $1CH_3$ contacts to Val26 $C_{\gamma1}H_3$ (weak; not shown) and Asp27 $C_\alpha H$ (moderate; see Figure 3K). However, additional, moderate intensity NOESY cross peaks to $1CH_3$ are observed (Figure 4A), including the C_βHs and NH of a TOCSY-detected NH C_α-$HC_\beta H_2$ fragment (see Supporting Information). The C_βHs of this backbone exhibit NOESY cross peaks (Figure 4D)

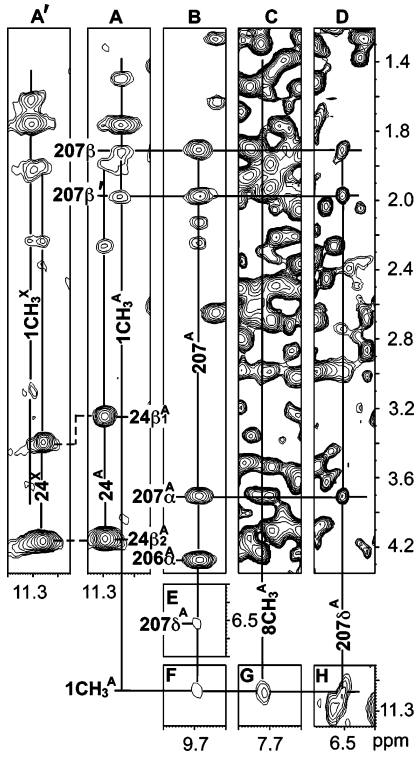

FIGURE 4: Portion of the ^1H NMR NOESY spectrum illustrating the contacts among His207 protons (B, D, E), between the His207 backbone and $1CH_3$ (A, F) and between the His207 ring and $1CH_3$ (H) for *Nm*HO^A-DMDH-CN. Note the absence of the His207 NOESY cross peak to $8CH_3$ in C; A′ exhibits the $1CH_3$ dipolar contact for *Nm*HO^X-DMDH-CN in ^1H_2O 100 mM in phosphate at pH 7.0 at 25 °C. The significant perturbation on the Asp24 $C_{\beta1}H$ shift in the 'A' → 'X' conversion is noted in A′ and A.

to the $C_\delta H$ of a TOCSY-detected (not shown) His ring, identifying a His in contact with $1CH_3$. This His exhibits properties very similar to that of a similar His in the PH complex, where it was in contact primarily with the $8CH_3$ and only very weakly with the $1CH_3$; it was assigned (*31*, *37*) to His207. In *Nm*HO-DMDH-CN, His207 fails to exhibit either $C_\beta H$ or $C_\delta H$ cross peaks to the $8CH_3$.

It is notable that the His207 $C_\alpha H$ and C_βHs exhibit temperature-dependent shifts indicative of significant upfield dipolar shifts, which make it even more remarkable that the peptide NH for His207 resonates at 9.7 ppm, a shift indicative of a much stronger than usual peptide NH H-bond (*51*, *52*). The low-field bias of His207 peptide NH (9.7 ppm) is only ~1 ppm smaller than that for the His141 NH, which is a known donor to a carboxylate (*31*, *22*). A strong His207 peptide NH NOESY cross peak to an apparent $C_\alpha H$ at 4.3 ppm (Figure 5B) with a small dipolar shift, which is tentatively assigned to Pro206 on the basis of the reported model (*37*), and a His207 NH cross peak to another labile proton at 8.24 ppm (not shown) argues for its assignment to the peptide NH of Arg208. Spectral congestion at ~8.2 ppm precludes locating any of the Arg208 nonlabile protons by either TOCSY or NOESY. As found in the case of the *Nm*HO^A-PH-CN complex (*31*, *37*), the *C*-terminus interacts directly with the substrate, but the exact mode of the interaction and its functional consequences for ligand affinity (see below) differ for PH and DMDH.

Resonance Assignments and Structural Characterization for NmHO^X-DMDH-CN. The DMDH and residue signals of

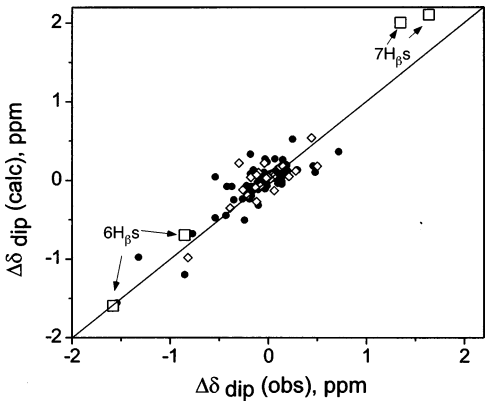

FIGURE 5: Plot of the predicted difference in dipolar shifts, $\Delta\delta_{dip}$(calc) (=δ_{dip}(calc); (*Nm*HO^A-PH-CN) − δ_{dip}(calc; *Nm*HO^A-DMDH-CN)), versus the differences in observed shift, $\Delta\delta_{DSS}$(obs) (= δ_{DSS}(obs; *Nm*HO^A-PH-CN) − δ_{DSS}(obs; *Nm*HO^A-DMDH-CN)). The common input data are shown as closed circles and propionate C$_\beta$Hs, and peptide NHs are shown as open diamonds and squares, respectively.

interest in *Nm*HO^X-DMDH-CN could be assigned on the same basis as that for the 'A' complex. The DMDH chemical shifts for the proximal helix are listed in Table 1, and the strongly dipolar-shifted proximal helix residue shifts are listed in Table 2, whereas the remaining assignments are provided in Supporting Information.

The most notable structural differences between *Nm*HO^A-DMDH-CN and *Nm*HO^X-DMDH-CN, as previously found for the same PH complexes (*37*), occur in the interaction of the *C*-terminus with the substrate. First, it was not possible to detect by TOCSY or NOESY a backbone or ring system in the X complex that exhibits a strong low-field bias for the NH and ring NOEs to the 1CH$_3$ (or 8CH$_3$) comparable to His207. The Asp27C$_\alpha$H NOESY cross peak to 1CH$_3$ is conserved (not shown), but there are only weak NOEs (Figure 4A′) in the spectral window, where the His207 C$_\beta$Hs exhibited NOESY cross peaks to 1CH$_3$ in *Nm*HO-DMDH-CN (Figure 4A). The retention of NOESY cross peaks to the 1CH$_3$ in *Nm*HO^A-DMDH-CN, which cannot be accounted for by the crystal structure (*22*), suggest the likelihood that in contrast to the PH complex (*37*), the His207 backbone interacts weakly with the substrate pocket in the vicinity of 1CH$_3$ even upon cleaving Arg208His209 in the 'X' complex.

It is noted that the effect of the 'A' → 'X' conversion on the substrate chemical shifts is somewhat larger for DMDH than that PH (compare data in Table 1). Moreover, two proximal residues Asp24 and Asp27, of which the latter has been proposed (*31*, *37*) to serve as the acceptor in the His207 peptide NH in *Nm*HO^A-PH-CN, exhibit significant chemical shift changes (Table 2 for Asp24), further supporting a significant difference in the *C*-terminus interaction with the proximal helix in the 'A' and 'X' complexes.

Magnetic Axes for NmHO^A-DMDH-CN. The solution molecular structure of the *Nm*HO^A-PH-CN complex for residues to Phe11 through Phe192 has been shown (*31*) to be conserved with respect to the *Nm*HO-PH-NO crystal structure (*22*), except for the 180° reorientations of the side chains of Gln49 about the $\gamma-\delta$ bond and His53 about the $\beta-\gamma$ bond. The conserved NOESY pattern for the *Nm*HO^A-DMDH-CN relative to that of the *Nm*HO^A-PH-CN complex supports an inconsequentially altered molecular structure for Phe11-Phe192 upon substituting DMDH for PH. The substrate as well as numerous residues, however, exhibits substantial differences in the hyperfine shift between the two complexes. The most likely origin of such large dipolar shift changes with a conserved molecular structure is a change in the orientation of the magnetic axes. Using the δ_{dip}(obs) for the *Nm*HO^A-DMDH-CN complex as input for the determination of the orientation of the magnetic axes, a good fit is obtained with $\alpha = 215 \pm 10°$, $\beta = 12 \pm 1°$, and $\kappa = 40 \pm 15°$ (not shown; see Supporting Information), which, when compared to those obtained for the PH complex with the same assignments ($\alpha = 200 \pm 10°$, $\beta = 8 \pm 1°$, and $\kappa = 40 \pm 10°$; not shown, see Supporting Information), indicate that only the tilt magnitude is significantly different in the PH and DMDH complexes, with the tilt ~4° larger with the DMDH than PH substrate. Although the propionate C$_\alpha$Hs shifts are dominated by the contact shifts (*46*), the C$_\beta$Hs are expected to exhibit negligible contact shifts. Indeed, the observed propionate C$_\beta$H hyperfine shift is quantitatively predicted by the magnetic axes (not shown; see Supporting Information).

The validity of attributing the residue shift difference between *Nm*HO^A-PH-CN and *Nm*HO^A-DMDH-CN overwhelmingly to a 4° larger tilt of the major magnetic axis (and hence, Fe-CN unit), rather than any significant change in molecular structure, is emphasized by the good correlation of the differences upon replacing PH with DMDH for the two complexes in the observed chemical shifts

$$\Delta\delta_{DSS}(\text{obs}) = \delta_{DSS}(\text{obs; } Nm\text{HO-PH-CN}) - \delta_{DSS}(\text{obs; } Nm\text{HO-DMDH-CN}) \quad (4)$$

and the predicted differences in dipolar shifts, $\Delta\delta_{dip}$(calc),

$$\Delta\delta_{dip}(\text{calc}) = \delta_{dip}(\text{calc; } Nm\text{HO-PH-CN}) - \delta_{dip}(\text{calc; } Nm\text{HO-DMDH-CN}) \quad (5)$$

given by the determined magnetic axes for the two complexes, as shown in Figure 5. Last, although the propionate C$_\beta$Hs exhibit very large shift changes between the PH and DMDH complexes, suggestive of major reorientation, the plot in Figure 5, in fact, shows that these substantial shift changes are completely consistent with the largely conserved propionate orientation but altered magnetic axes.

Cyanide Affinities for NmHO^A-DMDH-CN and NmHO^X-DMDH-CN. The heme methyl signals for high-spin *Nm*HO^A-DMDH-H$_2$O and *Nm*HO^X-DMDH-H$_2$O are not resolved (*50*) such that only the heme methyl signals of the cyanide complex yield information on the relative values of the cyanide binding constant in the reaction *Nm*HO-PH-H$_2$O + CN$^-$ → *Nm*HO-PH-CN + H$_2$O, given by

$$K^i_{eq} = [Nm\text{HO}^i\text{-DMDH-CN}]/[Nm\text{HO}^i\text{-DMDH-H}_2\text{O}][\text{CN}^-] \quad (6)$$

where i = A or X. A sample that is ~3:10 *Nm*HO^A-DMDH-H$_2$O/*Nm*HO^X-DMDH-H$_2$O exhibits comparable intensities for *Nm*HO^A-PH-CN and *Nm*HO^X-PH-CN at low CN$^-$ concentration (not shown; see Supporting Information), indicating that K_{eq} in eq 6 is ~3.3. This difference between the 'A' and 'X' species is a factor ~2 times larger than that observed with PH as substrate (*37*).

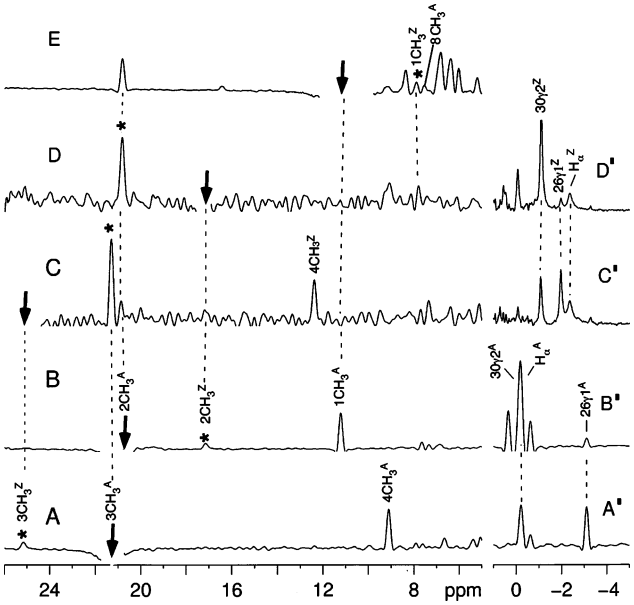

FIGURE 6: NOESY slices (A−E, A′, B′) and steady-state NOEs (C′, D′) through pyrroles A and B methyls in the equilibrium mixture *Nm*HO^{A}-DMDH-CN (~90%) and *Nm*HO^{Z}-DMDH-CN (~10%), in 100 mM phosphate at pH 7.0 at 25 °C. The cross peaks corresponding to saturation−transfer by chemical exchange, rather than NOEs, are marked by asterisks. NOESY slices through 3CH$_3^A$ with (A) NOE to 4CH$_3^A$ and saturation−transfer to 3CH$_3^Z$ and (A′) NOE to α-meso-H, Val26 $C_{\gamma 1}H_3$ and Val30 $C_{\gamma 2}H_3$. NOESY slice through (B) 2CH$_3^A$ with NOE to 1CH$_3^A$ and saturation−transfer to 2CH$_3^Z$, and (B′) NOE to α-meso-H, Val26 $C_{\gamma 1}H_3$, and Val30 $C_{\gamma 2}H_3$. (C) NOESY slice through 3CH$_3^Z$ with NOE to 4CH$_3^Z$ and saturation−transfer to 3CH$_3^A$, and (C′) steady-state NOE upon saturating 3CH$_3^Z$, to α-meso-H^Z, Val26^Z$C_{\gamma 1}H_3$, and Val30^Z$C_{\gamma 2}H_3$; (D) NOESY slice through 2CH$_3^Z$ with NOE to 1CH$_3^Z$ and saturation−transfer to 2CH$_3^A$, and (D′) steady-state NOE upon saturating 2CH$_3^Z$, to α-meso-H, Val26^Z$C_{\gamma 1}H_3$, and Val30^Z$C_{\gamma 2}H_3$; and (E), NOESY slice through 1CH$_3^A$ with NOE to 2CH$_3^A$ and saturation−transfer to 1CH$_3^Z$.

NmHO^Z-DMDH-CN. The use of the symmetric hemin, DMDH, leads to an equilibrium molecular structural heterogeneity for species 'A', whose position depends on the phosphate concentration. As shown in Figure 2B and B′, a decrease in phosphate concentration leads to a sharp increase in the population of species Z at the expense of species A. Because it is an equilibrium heterogeneity (see below), the polypeptide in A and Z must be identical, that is, Ser2-His209. The signals for all peaks of species Z are broader than those for the A or X species, precluding the complete assignment of DMDH and severely limiting assignment of active site residues in this complex. However, as shown below, the dynamics of the A ↔ Z equilibrium are such as to allow the transfer of assignments for key substrate and residue signals for resolved *Nm*HO^A-DMDH-CN signals to *Nm*HO^Z-DMDH-CN by chemical exchange.

Figure 6 illustrates NOESY slices through methyl diagonals that assign pyrrole A and B substituents. Cross peaks due to chemical exchange (*53*) (as determined by their temperature-dependent intensities), rather than NOEs, are labeled with asterisks. The NOESY slices through the 'A' species, 3CH$_3^A$ and 2CH$_3^A$, confirm the NOEs to the adjacent 4CH$_3^A$ and 1CH$_3^A$, respectively, and yield the 3CH$_3^Z$ and 2CH$_3^Z$ assignments by magnetization-transfer, as shown in Figure 6A and B, respectively. Similarly, slices through the 'Z' species 3CH$_3^Z$ and 2CH$_3^Z$ yield NOEs to the 4CH$_3^Z$ and 1CH$_3^Z$ peaks, as illustrated in Figures 6C and D, respectively. The 1CH$_3^Z$ NOE in Figure 6D is confirmed by the NOESY slice through 1CH$_3^A$ (Figure 6E), which exhibits 1CH$_3^Z$ by magnetization transfer. The available DMDH assignments for species Z are included in Table 1. The upfield portion of Figures 6A′ and B′ yield the NOESY cross peak pattern for species 'A' to α-meso-H and the methyls of Val26 $C_{\gamma 1}H_3$ and Val30 $C_{\gamma 2}H_3$ that are very close to those expected on the basis of the crystal structure with the 2,4-vinyls replaced by methyls groups. Weak NOESY cross peaks from the resolved Val26 $C_{\gamma 1}H_3$ and Val30 $C_{\gamma 2}H_3$ peaks of species 'A', which show intensity increases with elevated temperature, assign the same Val methyl peaks in species Z′ (not shown; labeled in Figure 6C′ and D′). The NOESY slices for the 'Z' species 2CH$_3^Z$ and 3CH$_3^Z$ to the upfield residues exhibited sensitivity that was too low to quantitate intensities. However, steady-state NOEs upon saturating 2CH$_3^Z$ (Figure 6D′) and 3CH$_3^Z$ (Figure 6C′) show essentially the same distribution of NOEs to the α-meso-H and Val26 and Val30 methyls as that observed for the same 'A' isomer methyls (Figures 6A′ and B′).

Attempts to locate the 'Z' species heme 5CH$_3^Z$ and 8CH$_3^Z$ peaks as well as propionate CH ^{Z} were fruitless because these broad methyl peaks are not resolved, and the weak exchange cross peaks to species 'A' could not be resolved from much stronger NOEs to nearly degenerate labile or aromatic ring protons. The only other key assignments, in addition to Val26 and Val30, that could be made include the His23 backbone and Thr20. One His23 $C_\beta H$ ^{Z} is partially resolved, and its intensity with phosphate concentration correlates with the resolved 2CH$_3^Z$ intensities (not shown). The axial His assignment is made on the basis of the observed His23 $C_\beta H$ NOESY cross peak to the $C_\alpha H$ of Thr20, an expected α_i-β_{i+3} connectivity, as is illustrated in Figure 7. The relative intensities of the two His23 C_βHs to Thr20 $C_\alpha H$ cross peaks provide the stereospecific assignment of the His23 β methylene protons. The partial DMDH and limited, but critical, amino acid residue chemical shifts for *Nm*HO^Z-DMDH-CN are included in Tables 1 and 2, respectively, where the data can be compared to those of the A and X species with DMDH.

Further assignments for the *Nm*HO^Z-DMDH-CN complex were not attainable by ^{1}H NMR because of the broader lines for the Z than A or X species. Although elevated temperature narrows the Z lines somewhat, it also causes much more rapid conversion of A, Z → X, even during the duration of a 2D spectrum. An inspection of ^{1}H NMR spectra of a completely converted *Nm*HO^X-DMDH-CN sample at 50 mM phosphate failed to give any evidence (not shown) for an additional set of methyl peaks in equilibrium with 3CH$_3^X$ or 2CH$_3^X$ (as observed for 3CH$_3^A$, 2CH$_3^A$; see Figure 6A and B). Hence, we conclude that species 'Z' for the Ser2-His209 polypeptide requires the *C*-terminal Arg208His209 to be detectably populated.

Activity of NmHO-DMDH. The product of reacting *Nm*HO-DMDH-H_2O with ascorbate and desferrioxamine yielded a single sharp peak by HPLC (*43*) (not shown) that can be safely attributed to the symmetric 2,4-dimethyl-α-biliverdin product.

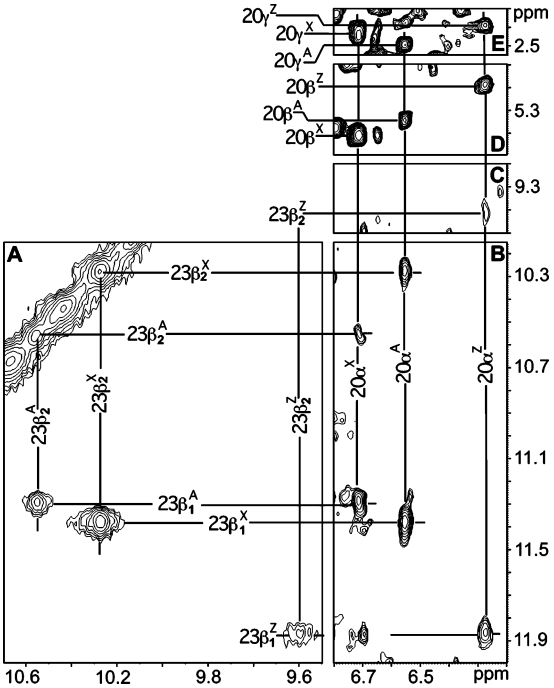

FIGURE 7: Portion of the NOESY spectrum (mixing time 40 ms; repetition rate 2 s^{-1}) of *Nm*HO-DMDH-CN in ^1H_2O, 50 mM in phosphate at pH 7.0 at 25 °C, which consists of 55% 'A', ~30% 'Z', and 15% 'X', illustrating the dipolar shifts among the His23 backbone and the Thr20 protons for each of the three species A, X, and Z, with cross peaks labeled with the applicable superscript; (A, B) intra-His23 backbone contacts; (B, C) α_i-β_{i+3} Thr20 to His23 contacts; and (C, D) intra-Thr20 contacts that stereospecifically assign the His23 C_βHs (His $C_{\beta 1}$H is predicted (*22*) to have the much stronger contact to Thr20 C_αH than for the His $C_{\beta 2}$H).

DISCUSSION

Molecular Structure. The pattern of intraresidue and residue−substrate NOESY cross peaks involving residues Phe11-Phe192 in *Nm*HO-DMDH-CN is essentially the same as that for *Nm*HO-PH-CN (*31*). The T_1s for resolved resonances (not shown) in the complexes are also indistinguishable for the two complexes. Except for the 180° rotation about the $\gamma-\delta$ bond for Gln49 and the $\beta-\gamma$ bond for His53 also observed in *Nm*HO-PH-CN (*31*) and *Nm*HO-PH-H_2O (*36*), the *Nm*HO-DMDH-CN structure for this portion is completely consistent with the crystal structure (*22*). The highly conserved structure encompasses all His residues, except for the *C*-terminal His207 and His209. The failure to detect and assign in *Nm*HO^A-DMDH-CN Gly120, which in *Nm*HO^A-PH-CN was strongly relaxed and strongly low-field hyperfine-shifted, (*31*) is readily accounted for by the altered magnetic axes, which lead to the prediction that the strongly relaxed Gly120 NH (and the weakly relaxed Ala122) signal resonates under the intense 5−10 ppm spectral window. Similarly, the Asp27 signals were predicted to be under the intense 0−5 ppm aliphatic envelope, and hence, Asp27 was not assignable in the PH complex (*31*). However, in the DMDH complex, Asp27 is shifted sufficiently further upfield so as to lead to a partially resolved C_αH for which the remaining side chain is readily detected by TOCSY/NOESY.

The conserved mean hyperfine shift for the His23 C_βHs in the DMDH and PH complexes argues for conservation of the axial His bond strength. The heme substituents exhibit somewhat different hyperfine shifts in the DMDH and PH complexes, but they are primarily contact in origin, and their asymmetry is modulated strongly by the differential rhombic perturbation of 2-,4-methyl replacing the 2-,4-vinyl groups (*46*). In fact, the crystallographic orientation (*22*) of the axial His imidazole plane relative to the N−Fe−N vector (ϕ in Figure 1) has $\phi \sim 45°$, which is completely consistent (*54*) with the nearly identical shifts within the heme methyl pairs $2CH_3/3CH_3$ and $5CH_3/8CH_3$. The pattern and intensities of NOESY cross peaks for the $3CH_3$ (Val26, Val30, Tyr184) and $5CH_3$ (Cys113) are similar in the PH and DMDH complexes (*31*), arguing against differences in the in-plane rotational position of PH and DMDH greater than ~5°. The difference in propionate C_αH shifts between the PH and DMDH complexes, due to the angular dependence of α-methylene protons (*46*), is consistent with as little as a 5° difference in the $C_\pi-C_\alpha$ (C_π is the aromatic ring carbon) bond rotational position for the two complexes. The significant differences in the dipolar shifts for nonligated residues can be explained quantitatively by a small (~4°), but important, increase in the tilt of the major magnetic axes that tilts in the DMDH than in the PH complex. Even the large changes in propionate C_βH shifts reflect the changed magnetic axes and the not so significantly altered propionate orientations in the heme pocket.

The tilt of the Fe-CN unit, which is correlated (*26*, *33*, *46*) with the tilt of the major magnetic axis *z* by β, results largely from the steric interaction of the ligand with the Gly120 backbone (*22*) because of the preferences for CN^- binding normal to the heme plane, in contrast to the bent $Fe-O_2$ structure, where the steric interaction only orients the direction of the terminal O in $Fe-O_2$ (*23*). Interestingly, the change of β in the PH → DMDH substitution is in the opposite direction of that found in similar hHO complexes (*55*), where it could readily be rationalized by the structural change expected upon reducing the bulk of the substrate in the vinyl → methyl substitution (*25*). A very plausible basis for this change in the Fe-CN tilt for *Nm*HO complexes will be considered (see below).

Nature of the C-Terminal Interaction with DMDH. As found for the PH complex (*36*, *37*), the native Ser2-His209 polypeptide results in a strong interaction between the heme periphery and one His residue that can only arise from the *C*-terminus His207-Arg208-His209 fragment. Because the position of Pro206 relative to the protein matrix in *Nm*HO-PH-H_2O could be shown (*36*) to be similar to that in the crystal structure (*22*), the modeling of the *C*-terminal interaction has shown that it is the peptide NH, and not the ring, of His207 that interacts with a proximal rather than distal side H-bond acceptor. The most likely proximal acceptor to the strong H-bond by the His207 peptide NH was deduced to be the Asp27 carboxylate (*37*). The major stabilization of the *C*-terminal interaction with substrate has been argued (*37*) to result from a salt bridge between the side chain of Arg208 and the 7-propionate carboxylate.

The data for the DMDH complex are consistent with a similar, but stronger interaction of the His207 peptide NH with Asp27 and Arg208 guanidyl groups with the 7-propionate. The stronger interaction between His207 and Asp27 is evidenced by a movement of the His207 from between the $8CH_3$ and $1CH_3$ (but closer to the former in the PH complex) to the closer proximity of $1CH_3$ and the stronger low-field bias of the His207 NH (9.7 ppm) relative to that

of the the PH complex (9.1 ppm), in spite of the fact that the magnetic axes for both complexes predict an upfield δ_{dip} for His207 (as observed for all backbone protons). Such a strong low-field bias is indicative of a stronger than usual H-bond (*51*, *52*). Second, the His207 peptide NH in *Nm*HO-PH-CN exhibited (*37*) significant saturation−transfer by exchange with bulk water (*53*), and the NH signal for Arg208 could not be detected (*37*), indicating relatively labile protons that reflect limited dynamic stability (*56*) in the *C*-terminal substrate interaction. In the present *Nm*HO-DMDH-CN complex, the degree of saturation−transfer and, hence, the lability of the His207 NH is significantly reduced, and the Arg208 NH is readily detected (not shown; see Supporting Information), arguing for an increased dynamic stability of the *C*-terminus interaction with the substrate in the DMDH relative to PH complex. Thus the interaction between the *C*-terminus and substrate in the DMDH complex is very similar to that in the PH complex, except that the *C*-terminus moves slightly closer to the His207 H-bond acceptor, Asp27.

An inspection of the *Nm*HO-PH-NO (*22*) crystal structure shows that the Asp27 side chain is in strong van der Waals contact with the 2-vinyl group, whose terminal methylene group is oriented toward the proximal side and, hence, could interfere with an "optimal" interaction between the carboxylate and the *C*-terminal His207 peptide NH. Upon decreasing this steric bulk on the proximal side by vinyl → methyl substitution in the DMDH complex, the Asp27 carboxylate appears to adopt an orientation that allows a stronger interaction with His207. The inability to detect the *C*-terminal His207Arg208His209 fragment in the crystal (*15*, *22*) and our demonstration (*37*) that the *C*-terminal Arg208His209 fragment is spontaneously cleaved in the PH complex with a half-life of ∼24 h strongly suggest the possibility that the reported crystal structures (*15*, *22*), in fact, are of the cleaved Ser2−His207 complex, and hence, the orientation of the Asp27 carboxylate in the native complex in solution may not reflect that observed in the crystal structures (*15*, *22*).

Interestingly, a stronger interaction of the *C*-terminus with Asp27 carboxylate in the DMDH than that in the PH complex would facilitate a small movement of the heme and proximal helix toward the *C*-terminus. A movement in this direction would force the Fe-CN ligand more strongly against the distal helix Gly120 backbone and, therefore, provide a rationalization for the ∼4° increased tilt of the FeCN unit toward the α-meso position in the DMDH over the PH complex.

Effect of Arg208His209 Cleavage. The conversion of the *Nm*HO^{A}-DMDH-CN complex (consisting of Ser2-His209) to *Nm*HO^{X}-DMDH-CN (consisting of Ser2-His207) is supported directly by the mass spectrometeric data that indicate a ∼289 Da mass unit loss, and retention of Ser2, precisely as observed (*37*) for the analogous PH complex. The rate of this A → X conversion is much more rapid (by factor of ∼5) than that for the PH complex (*37*), with significant conversion detected even within a 24 h 2D NMR experiment. The 2D spectra indicate a conserved molecular structure for the portion Phe11-Phe192 in the A → X conversion, with only a small influence in δ_{dip}(obs) for strongly shifted proximal and distal helix residues. The differences in δ_{dip}(obs) for the A and X complexes do not allow interpretation on the basis of systematic small changes in one of the parameters in the magnetic axes. The changes in active site residue hyperfine shifts in the 'A' → 'X' conversion in the present DMDH complex are larger than those observed in the 'A' → 'X' conversion of the PH complex (*37*), and this probably reflects the stronger interaction between the *C*-terminus and the substrate in the DMDH than that in the PH complex.

The most conspicuous difference in the 2D NMR spectra of the 'A' and 'X' complexes occurs for the contacts between the *C*-terminus and substrate $1CH_3$, as shown in Figure 4. The strongly low-field shifted NH for the His207 peptide is not detectable, and the strong NOESY cross peaks between $1CH_3$ and the His207 backbone are lost. However, the $1CH_3$, even *Nm*HO^{X}-DMDH-CN, exhibits more NOESY cross peaks than is consistent with predictions by the crystal structure (*22*). The retention of such NOESY cross peaks to the $1CH_3$ in the 'X' complex of DMDH is in sharp contrast to the same conversion for the PH complex where the crystallographically unexpected His207 cross peaks to $8CH_3$ are completely lost in the same 'A' → 'X' conversion (*37*). This retention of weaker cross peaks in the aliphatic region to $1CH_3$ in *Nm*HO^{X}-DMDH-CN suggests the possibility that some weaker interaction between His207 and the Asp27 carboxylate is retained in the cleaved X complex. Such retained interaction in the 'X' complex could occur because the replacement of the bulky 2-vinyl with a methyl allows an Asp27 side chain orientation that favors an interaction with His207 in the DMDH over the PH complex. Finally, the stronger interaction of the *C*-terminus with the substrate in the DMDH than that in the PH complex is supported not only by the stronger H-bond between Asp27 and His207 and slower exchange rates of the labile protons but also by the significantly larger difference in the CN^- affinity between the 'A' and 'X' complexes in DMDH (factor ∼3.3) than that in the PH (factor ∼1.7) complexes.

The apparent sensitivity of the *C*-terminal interaction with the substrate and proximal helix to substitution on the substrate raises the possibility that the interaction of the *C*-terminus with the active site is modulated during the enzyme reaction. While α-meso-hydroxylation may not significantly alter the orientation of the 2-vinyl group, the two subsequent intermediates, in particular, ferric biliverdin, can be expected to alter the 2-vinyl interaction with the proximal helix, as suggested in the crystal structure of the PH and ferric biliverdin of rat HO (*14*, *26*, *57*). It has been observed that the cleaved *Nm*HO (Ser2-His207) more readily releases biliverdin than WT *Nm*HO (Ser2-His209) (*37*).

*Molecular Nature of Species Z. Nm*HO^{Z}-DMDH-CN is in dynamic equilibrium with *Nm*HO^{A}-DMDH-CN and, hence, consists of Ser2-His209. Its population is enhanced at low phosphate concentration, which may reflect either a salt effect on some unspecified salt-bridge or a specific binding of phosphate in the native complex; the nature of this interaction was not pursued further. Species 'Z' is not likely physiologically relevant because it appears solely with DMDH and not with native PH. However, species 'Z' is an interesting spectroscopic curiosity that provides key insight into the limitations of using heme methyl contact shift patterns (*27*, *54*, *58*) to conclude the detailed in-plane seating of a heme as relevant to the stereoselectivity of the HO reactions without explicit considerations of the orientation of the axial His ring (see below).

The failure to detect at low phosphate concentration an equilibrium species with either *Nm*HO^{X}-DMDH-CN or

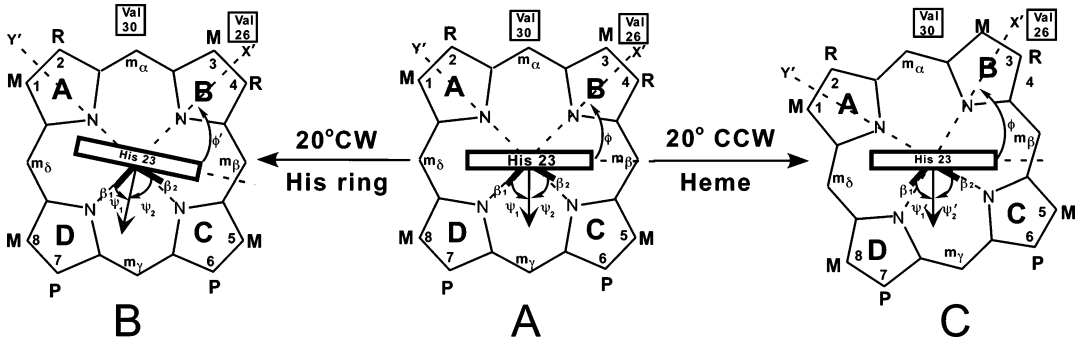

FIGURE 8: Schematic depiction of the orientation of the heme relative to the protein matrix represented by Val26 and Val30 of the proximal helix and to the axial His as represented by the angle ϕ between the His23 imidazole plane and the x' axis passing through the pyrrole B and D nitrogens; (A) as found in the crystal structure for *Nm*HO-PH-NO (*22*) and upon either (B) rotating the axial His23 imidazole plane ~20° clockwise relative to heme, with a conserved heme and axial His backbone positions relative to the protein matrix or (C) rotating the heme ~20° counter-clockwise about the heme normal with a conserved axial His orientation relative to the protein matrix. The positions of the His23 C_βHs are shown, defined by angles Ψ_1 and Ψ_2 for $C_{\beta 1}H$ and $C_{\beta 2}H$, respectively, with respect to the normal to the His23 imidazole plane.

*Nm*HO^A-PH-CN argues for an involvement of both the *C*-terminus and, indirectly, the 2-vinyl group in the formation of species Z. A plausible molecular model for species Z is gleaned from consideration of the difference in DMDH methyl and axial His C_βH hyperfine shifts between the A and Z complexes. The dominant contact shift pattern of the heme methyl directly reflects the orientation of the heme N−Fe−N vector relative to the axial His imidazole plane (*54*), given by the angle ϕ in Figures 1 and 8A. An empirical correlation between methyl contact shift and the angle ϕ for an electronically essentially centrosymmetric hemin have been presented (*54*), and it is noted that the A → Z conversion results in increased $3CH_3$ and $4CH_3$ shifts and decreased $1CH_3$ and $2CH_3$ shifts (see Table 1), as expected for an angle ϕ increased by ~20° in the A → Z conversion by either a clockwise rotation of the axial His (viewed from the proximal side) imidazole plane, as depicted in Figure 8B with a conserved seating of DMDH relative to the protein matrix, or by a counter-clockwise rotation of the DMDH relative to the conserved axial His imidazole orientation relative to the protein matrix, as depicted in Figure 8C.

An inspection of the steady-state NOEs between the $3CH_3$/$2CH_3$ and Val26/Val30 in *Nm*HO^Z-DMDH-CN (Figure 6C′ and D′) with the same NOESY slices for $3CH_3$/$2CH_3$ to Val26/Val30 in *Nm*HO^A-DMDH-CN (Figure 6A′ and B′) reveal essentially the same distribution of NOEs between the substrate and the two heme pocket Val residues arguing against any significant changes in the positions of DMDH relative to the protein matrix in the A and Z complexes. Hence, it must be the axial His imidazole orientation that is different in the A and Z species.

The β-methylene proton of the axial His23, like the α-methylene proton of the heme propionate in its interaction with the π-spin density of the attached aromatic ligand, exhibits contact shifts according to the following relationship (*46*):

$$\delta_{con} = B \cos^2\Psi, \qquad (7)$$

where B is a constant at a given temperature, and Ψ is the dihedral angle between the H−C−C_π plane and the normal to the π-system. The angle Ψ_1 and Ψ_2 in Figure 8 represent these dihedral angles for the stereospecifically assigned $C_{\beta 1}H$ and $C_{\beta 2}H$, respectively, of His23 based on the crystal structure (*22*). In the *Nm*HO-PH-NO crystal structure, these two angles are Ψ_1 ~55° and Ψ_2 = 65°, which are qualitatively consistent with the larger δ_{hf} for $C_{\beta 1}H$ than that for $C_{\beta 2}H$. A comparison of the His C_βH chemical shifts for the A and Z complexes reveals that the $C_{\beta 1}H$ experiences a significantly larger, and $C_{\beta 2}H$ a significantly smaller, low-field hyperfine shift in the Z complex rather than that in the A complex. An inspection of Figure 8A and C shows that a clockwise rotation of the His23 imidazole plane in the Z, relative to the A, complex indeed will involve a significant decrease in Ψ_1 for $C_{\beta 1}H$ and an increase in Ψ_2 for $C_{\beta 2}H$ in the Z relative to the A complex, as is clearly observed. A more quantitative analysis to estimate the angle of rotation is not possible at this time because the magnetic axes and, hence, dipolar shifts for complex Z are not known. Nevertheless, the present data clearly show that it is the axial His imidazole plane, and not the heme, whose orientation relative to the conserved protein matrix is altered in the dynamic interconversion between A and Z. The enzyme assay on the *Nm*HO-DMDH-complex affords a single isomer that was not identified but can be safely assumed to be the α-cleaved biliverdin. The absence of any other isomer biliverdin is consistent with the maintenance of the essentially conserved orientation of the substrate with the active site in both species A and Z.

The pattern of substrate methyl contact shifts is frequently used to determine the exact seating of PH relative to the protein matrix (*27*, *58*), and this seating can influence the stereoselectivity of the PH cleavage. It has been tacitly assumed (*59*) that the axial His orientation is strongly conserved among different HOs or for the mutants of a given HO. In general, the signals for the axial His C_βHs are not assigned, and hence, it is not known whether the axial His orientation has changed. The present results demonstrate the potential pitfalls of assuming a solely PH orientation without explicitly considering the reorientation of the axial His.

The nature of the structural change that accounts for the DMDH methyl contact shift pattern in species Z yields a clue as to the structural basis for the altered axial His imidazole plane orientation. Crystal structures of both mammalian (*13*, *14*) and bacterial (*16*) HO complexes show that the axial His imidazole orientation is stabilized by an acidic side chain at position $i + 4$ (where i is the axially ligated His) of the proximal helix serving as acceptor to the

His imidazole ring $N_\delta H$. *Nm*HO is an exception to this (*15*, *22*) in that the His23 ring $N_\delta H$ is donor to the carboxylate of the adjacent Asp24 and not the expected Asp27. This switch in the H-bond acceptor to the ligated His in *Nm*HO has been proposed (*31*) to free Asp27 to serve as acceptor to the *C*-terminal His207 peptide NH. The significant change in the orientation of the axial His imidazole plane in the A → Z conversion, therefore, suggests a rupture of the Asp24 side chain to His23 ring H-bond. Such a rupture could occur because the His207 NH in species Z utilizes the Asp24 carboxylate as the alternate acceptor. The facilitation of the interaction to form species Z upon replacement of the vinyl with methyl could be rationalized on the basis of the diminished proximal side steric blocking of access to the Asp24 carboxylate.

The loss of Arg208His209 in species X results in a decrease in the cyanide affinity by a factor of ~3.3, which is larger than the factor of ~1.7 observed (*37*) for the PH complex. The larger effect on CN^- affinity for DMDH than that for PH likely originates in the significantly stronger interaction between the *C*-terminus and the substrate pocket in the complex of DMDH. Similarly, the faster (by a factor of ~5) cleavage of the Arg208His209 dipeptide for DMDH compared to that for PH (*37*) may also result from some change in the His207−Arg208 bond upon PH → DMDH conversion. A more detailed interpretation of the cleavage rate must await planned mechanistic studies. A possible origin of the A ⇔ Z equilibrium and the interconversion barrier is a cis−trans isomerization of Pro206 in the *C*-terminus that is induced by the stronger interaction of the *C*-terminus with the active site in the DMDH relative to that in the PH complex. A more quantitative description of the interaction of the *C*-terminus with the active site in *Nm*HO-DMDH complexes would require a $^{15}N/^{13}C$-labeled sample. However, the half-life for the Arg208His209 dipeptide cleavage is ~24 h for the *Nm*HO-DMDH-CN complex in solution, which is significantly shorter than the duration required for 3D NMR experiments (72 h). Hence, the factors (pH, ionic strength, and buffer) influencing the rate of A → X conversion for the DMDH complexes will have to be explored first to see if it is possible to extend the half-life of the A → X conversion.

CONCLUSIONS

The interaction between the *C*-terminus and substrate in *Nm*HO complexes differs for protohemin and 2,4-dimethyldeuterohemin, with the *C*-terminus more strongly penetrating the heme cavity for the latter substrate. This effect is attributed to the 2-vinyl group interfering with optimal orientation of the Asp27 carboxylate for serving as H-bond donor to the His207 peptide NH. This conclusion is supported by the greater dynamic stability (slower H-bond donor exchange rates) of the *C*-terminus−substrate interaction and a slightly larger tilt of the Fe-CN unit (major magnetic axis) toward the α-meso position. The differential *C*-terminal interaction with substrate substituents suggests variable interaction of the *C*-terminus with the intermediates in the HO reaction.

A similar "spontaneous" cleavage of the *C*-terminal Arg208His209 dipeptide of *Nm*HO is observed for the 2,4-dimethyldeuterohemin as for the protohemin complex, but the rate is faster by a factor of ~5 for the former substrate, suggesting a correlation between the strength of the *C*-terminal interaction with substituents and the rate of this cleavage reaction. The cleavage of Arg208His209 has a greater effect on the CN^- affinity in DMDH than in PH, again supporting a strong *C*-terminal interaction with the substrate for DMDH than that for PH.

Finally, an equilibrium isomer for the DMDH complex is induced at low phosphate concentration for the *Nm*HO-DMDH complex. This complex exhibits a significantly perturbed heme methyl hyperfine shift pattern that is shown to arise not from a change in the orientation of the substrate relative to the protein matrix but from a rotation of the axial His imidazole ring relative to a conserved substrate orientation and protein matrix. These observations underscore the need to consider axial His orientation before interpreting heme methyl hyperfine shift patterns in terms of substrate orientation as relevant to the stereoselectivity of the ring cleavage.

SUPPORTING INFORMATION AVAILABLE

Mass spectra for *Nm*$HO^{A,X}$-DMDH-CN complexes, NMR of CN^- titration of *Nm*$HO^{A,X}$-DMDH-H_2O, NOESY spectra for inter-DMDH and peptide backbone contacts and upfield TOCSY spectra for *Nm*HO^A-DMDH-CN, NOESY spectra of NH contacts for *Nm*HO^X-DMDH-CN, and plots of δ_{dip}-(calc) vs δ_{dip}(obs) for magnetic axis for *Nm*HO^A-PH-CN and *Nm*HO^A-DMDH-CN and the chemical shifts of assigned residues. This material is available free of charge via the Internet at http://pubs.acs.org.

REFERENCES

1. Tenhunen, R., Marver, H. S., and Schmid, R. (1969) Microsomal heme oxygenase. Characterization of the enzyme, *J. Biol. Chem. 244*, 6388−6394.
2. Ortiz de Montellano, P. R., and Auclair, K. (2003) Heme Oxygenase Structure and Mechanism, in *The Porphryin Handbook* (Kadish, K. M., Smith, K. M., and Guilard, R., Eds.) pp 175−202, Elsevier Science, San Diego, CA.
3. Uzel, C., and Conrad, M. E. (1998) Absorption of heme iron, *Semin. Hematol. 35*, 27−34.
4. Maines, M. D. (1997) The heme oxygenase system: A regulator of second messenger gases, *Annu. Rev. Pharmacol. Toxicol. 37*, 517−554.
5. Beale, S. I. (1994) Biosynthesis of open-chain tetrapyrroles in plants, algae, and cyanobacteria, *Ciba Found. Symp. 180*, 156−168.
6. Schmitt, M. P. (1997) Utilization of host iron sources by *Corynebacterium dihtheriae*: identification of a gene whose product is homologous to eukaryotic heme oxygenases and is required for acquisition of iron from heme and hemoglobin, *J. Bacteriol. 179*, 838−845.
7. Zhu, W., Willks, A., and Stojiljkovic, I. (2000) Degradation of heme in gram-negative bacteria: the product of the hemO gene of Neisseriae is a heme oxygenase, *J. Bacteriol. 182*, 6783−6790.
8. Ratliff, M., Zhu, M., Deshmukh, R., Wilks, A., and Stojiljkovic, I. (2001) Homologues of Neisserial heme oxygenase in gram-negative bacteria: Degradation of heme by the product of the pigA gene of *Pseudomonas aeruginosa*, *J. Bacteriol. 183*, 6394−6403.
9. Yoshida, T., and Migita, C. T. (2000) Mechanism of heme degradation by heme oxygenase, *J. Inorg. Biochem. 82*, 33−41.
10. Wilks, A. (2002) Heme oxygenase: Evolution, structure, and mechanism, *Antioxidants Redox Signal 4*, 603−614.
11. Frankenberg-Dinkel, N. (2004) Bacterial Heme Oxygenases, *Antoxid. Redox Signaling 6*, 825−834.
12. Rivera, M., and Zeng, Y. (2005) Heme Oxygenase, steering dioxygen activation toward heme hydroxylation, *J. Inorg. Biochem. 99*, 337−354.

13. Schuller, D. J., Wilks, A., Ortiz de Montellano, P. R., and Poulos, T. L. (1999) Crystal structure of human heme oxygenase-1, *Nat. Struct. Biol. 6*, 860−867.
14. Sugishima, M., Omata, Y., Kakuta, Y., Sakamoto, H., Noguchi, M., and Fukuyama, K. (2000) Crystal structure of rat heme oxygenase-1 in complex with heme, *FEBS Lett. 471*, 61−66.
15. Schuller, D. J., Zhu, W., Stojiljkovic, I., Wilks, A., and Poulos, T. L. (2001) Crystal structure of heme oxygenase from the Gram-negative pathogen *Neisseria meningitidis* and a comparison with mammalian heme oxygeanse-1, *Biochemistry 40*, 11552−11558.
16. Hirotsu, S., Chu, G. C., Unno, M., Lee, D.-S., Yoshida, T., Park, S.-Y., Shiro, Y., and Ikeda-Saito, M. (2004) The crystal structures of the ferric and ferrous forms of the heme complex of HmuO, a heme oxygenase of *Corynebacterium diphtheriae*, *J. Biol. Chem. 279*, 11937−11947.
17. Friedman, J., Lad, L., Li, H., Wilks, A., and Poulos, T. L. (2004) Structural basis for novel δ-regioselective heme oxygenation in the opportunistic pathogen *Pseudomonas aeruginosa*, *Biochemistry 43*, 5239−5245.
18. Ortiz de Montellano, P. R. (1998) Heme oxygenase mechanism: Evidence for an electrophilic, ferric peroxide species, *Acc. Chem. Res. 31*, 543−549.
19. Davydov, R. M., Yoshida, T., Ikeda-Saito, M., and Hoffman, B. M. (1999) Hydroperoxy-heme oxygenase generated by cryoreduction catalyzes the formation of α-*meso*-hydroxyheme as detected by EPR and ENDOR, *J. Am. Chem. Soc. 121*, 10656−10657.
20. Davydov, R., Kofman, V., Fujii, H., Yoshida, T., Ikeda-Saito, M., and Hoffman, B. M. (2002) Catalytic mechanism of heme oxygenase through EPR and ENDOR of cryoreduced oxy-heme oxygenase and its Asp 140 mutants, *J. Am. Chem. Soc. 124*, 1798−1808.
21. Wilks, A., Torpey, J., and Ortiz de Montellano, P. R. (1994) Heme oxygenase (HO-1) - Evidence for electrohpilic oxygen addition to the porphyrin ring in the formation of alpha-meso-hydroxyheme, *J. Biol. Chem. 269*, 29553−29556.
22. Friedman, J. M., Lad, L., Deshmukh, R., Li, H. Y., Wilks, A., and Poulos, T. L. (2003) Crystal structures of the NO- and CO-bound heme oxygenase from Neisseriae meningitidis - Implications for O2 activation, *J. Biol. Chem. 278*, 34654−34659.
23. Unno, M., Matsui, T., Chu, G. C., Coutoure, M., Yoshida, T., Rousseau, D. L., Olson, J. S., and Ikeda-Saito, M. (2004) Crystal structure of the dioxygen-bound heme oxygenase from *Corynebacterium diphtheriae*, *J. Biol. Chem. 279*, 21055−21061.
24. Lad, L., Wang, J., Li, H., Friedman, J., Bhaskar, B., Ortiz de Montellano, P. R., and Poulos, T. L. (2003) Crystal structures of the ferric, ferrous and ferrous-NO forms of the Asp140Ala mutant of human heme oxygenase-1: Catalytic implications, *J. Mol. Biol. 330*, 527−538.
25. Sugishima, M., Sakamoto, H., Noguchi, M., and Fukuyama, K. (2003) Crystal structures of CO-, CN-, and NO-bound forms of rat heme oxygenase-1 (HO-1) in complex with heme: Structural implications for discrimination between CO and O2 in HO-1, *Biochemistry 42*, 9898−9905.
26. Sugishima, M., Sakamoto, H., Higashimoto, Y., Omata, Y., Hayashi, S., Noguchi, M., and Fukuyama, K. (2002) Crystal structure of rat heme oxygenase-1 in complex with heme bound to azide: Implication for regiospecific hydroxylation of heme at the α-*meso* carbon, *J. Biol. Chem.* 45086−45090.
27. Caignan, G. A., Deshmukh, R., Wilks, A., Zeng, Y., Huang, H.-W., Moenne-Loccoz, P., Bunce, R. A., Eastman, M. A., and Rivera, M. (2002) Oxidation of heme to β- and δ-biliverdin by *Pseudomonas aeruginosa* heme oxygenase as a consequence of an unusual seating of the heme, *J. Am. Chem. Soc. 124*, 14879−14892.
28. Hernández, G., Wilks, A., Paolesse, R., Smith, K. M., Ortiz de Montellano, P. R., and La Mar, G. N. (1994) Proton NMR investigation of substrate-bound heme oxygenase: Evidence for electronic and steric contributions to stereoselective heme cleavage, *Biochemistry 33*, 6631−6641.
29. Gorst, C. M., Wilks, A., Yeh, D. C., Ortiz de Montellano, P. R., and La Mar, G. N. (1998) Solution ^{1}H NMR investigation of the molecular and electronic structure of the active site of substrate-bound human heme oxygenase: The nature of the distal hydrogen bond donor to bound ligands, *J. Am. Chem. Soc. 120*, 8875−8884.
30. Li, Y., Syvitski, R. T., Chu, G. C., Ikeda-Saito, M., and La Mar, G. N. (2003) Solution ^{1}H NMR investigation of the active site molecular and electronic structures of the substrate-bound, cyanide-inhibited bacterial heme oxygenase from *C. diphtheriae*, *J. Biol. Chem. 279*, 6651−6663.
31. Liu, Y., Zhang, X., Yoshida, T., and La Mar, G. N. (2004) ^{1}H NMR characterization of the solution active site structure of substrate-bound, cyanide-inhibited heme oxygenase from *Neisseria meningitidis*; Comparison to crystal structures, *Biochemistry 43*, 10112−10126.
32. Ortiz de Montellano, P. R. (1987) Control of the catalytic activity of prosthetic heme by the structure of hemoproteins, *Acc. Chem. Res. 20*, 289−294.
33. Li, Y., Syvitski, R. T., Auclair, K., Wilks, A., Ortiz de Montellano, P. R., and La Mar, G. N. (2002) Solution NMR characterization of an unusual distal H-bond network in the active site of the cyanide-inhibited, human heme oxygenase complex of the symmetric substrate, 2, 4-dimethyldeuterohemin, *J. Biol. Chem. 277*, 33018−33031.
34. Syvitski, R. T., Li, Y., Auclair, K., Ortiz de Montellano, P. R., and La Mar, G. N. (2002) ^{1}H NMR detection of immobilized water molecules within a strong hydrogen-bonding network in the distal side of substrate-bound human heme oxygenase, *J. Am. Chem. Soc. 124*, 14296−14297.
35. Li, Y., Syvitski, R. T., Auclair, K., Ortiz de Montellano, P. R., and La Mar, G. N. (2003) Solution ^{1}H, ^{15}N NMR spectroscopic characterization of substrate-bound cyanide-inhibited, human heme oxygenase: Water occupation of the distal cavity, *J. Am. Chem. Soc. 125*, 13392−13403.
36. Liu, Y., Zhang, X., Yoshida, T., and La Mar, G. N. (2005) Solution ^{1}H NMR characterization of the distal H-bond network and the effective axial field in the resting-state, high-spin ferric, substrate-bound complex of heme oxygenase from *N. meningitidis*, *J. Am. Chem. Soc. 127*, 6409−6422.
37. Liu, Y., Ma, L.-H., Satterlee, J. D., Zhang, X., Yoshida, T., and La Mar, G. N. (2006) Characterization of the spontaneous "aging" of the heme oxygenase from the pathological bacterium *Neisseria meningitidis* via cleavage of the C-terminus in contact with the substrate: Implications for functional studies and the crystal structure, *Biochemistry 45*, 3875−3886.
38. Zeng, Y., Caignan, G. A., Bunce, R. A., Rodriguez, J. C., Wilks, A., and Rivera, M. (2005) Azide-inhibited bacterial heme oxygenases exhibit an S=3/1 $(d_{xz}, d_{yz})^3(d_{xy})^1(d_z{}^2)^1$ spin state: Mechanistic implications for heme oxidation, *J. Am. Chem. Soc. 127*, 9794−9807.
39. Johnston, P. D., Figueroa, N., and Redfield, A. G. (1979) Real-time solvent exchange studies of the imino and amino protons of yeast phenylalanine transfer RNA by Fourier transform NMR, *Proc. Natl. Acad. Sci. U.S.A. 76*, 3130−3134.
40. Jeener, J., Meier, B. H., Bachmann, P., and Ernst, R. R. (1979) Investigation of exchange processes by two dimensional NMR spectroscopy, *J. Chem. Phys. 71*, 4546−4553.
41. Griesinger, C., Otting, G., Wüthrich, K., and Ernst, R. R. (1988) Clean TOCSY for ^{1}H spin system identification in macromolecules, *J. Am. Chem. Soc. 110*, 7870−7872.
42. Bax, A., and Davis, D. G. (1985) Mlev-17-based two-dimensional homonuclear magnetization transfer spectroscopy, *J. Magn. Reson. 65*, 355−360.
43. Zhang, X., Fujii, H., Matera, M., Migita, C. T., Sun, D., Sato, M., Ikeda-Saito, M., and Yoshida, T. (2003) Stereoselectivity of each of the three steps of the heme oxygenase reaction: hemin to *meso*-hydroxyhemin, *meso*-hydroxyhemin to verdoheme, and verdoheme to biliverdin, *Biochemistry 42*, 7418−7426.
44. Williams, G., Clayden, N. J., Moore, G. R., and Williams, R. J. P. (1985) Comparison of the solution and crystal structures of mitochondrial cytochrome *c*. Analysis of paramagnetic shifts in the nuclear magnetic resonance spectrum of ferricytochrome *c*, *J. Mol. Biol. 183*, 447−460.
45. Emerson, S. D., and La Mar, G. N. (1990) NMR determination of the orientation of the magnetic susceptibility tensor in cyano met-myoglobin: A new probe of steric tilt of bound ligand, *Biochemistry 29*, 1556−1566.
46. La Mar, G. N., Satterlee, J. D., and de Ropp, J. S. (2000) NMR of Hemoproteins, in *The Porphyrins Handbook* (Kadish, K. M., Smith, K. M., and Guilard, R., Eds.) pp 185−298, Academic Press, San Diego, CA.
47. Cross, K. J., and Wright, P. E. (1985) Calibration of ring-current models for the heme ring, *J. Magn. Reson. 64*, 220−231.
48. Neal, S., Nip, A. M., Zhang, H., and Wishart, D. S. (2003) Rapid and accurate calculation of protein ^{1}H, ^{13}C and ^{15}N chemical shifts, *J. Biomol. NMR 26*, 215−240.

49. Wüthrich, K. (1986) *NMR of Proteins and Nucleic Acids*, Wiley & Sons, New York.
50. Ma, L.- H., Liu, Y., Zhang, X., Yoshida, T., and La Mar, G. N. (2006) Modulation of the axial water hydrogen-bonding properties by chemical modification of the substrate in resting state, substrate-bound heme oxygenase from *N. meningitidis*; Coupling to the distal H-bond network via ordered water molecules, *J. Am. Chem. Soc. 128*, 6391−6399.
51. Wagner, G., Pardi, A., and Wüthrich, K. (1983) Hydrogen bond length and ^{1}H NMR chemical shifts in proteins, *J. Am. Chem. Soc. 105*, 5948−5949.
52. Harris, T. K., and Mildvan, A. S. (1999) High-precision measurement of hydrogen bond lengths in proteins by nuclear magnetic resonance methods, *Proteins: Struct., Funct., Genet. 35*, 275−282.
53. Sandström, J. (1982) *Dynamic NMR Spectroscopy*, Academic Press, New York.
54. Shokhirev, N. V., and Walker, F. A. (1998) The effect of axial ligand plane orientation on the contact and pseudocontact shifts of low-spin ferriheme proteins, *J. Biol. Inorg. Chem. 3*, 581−594.
55. Zhu, W., Li, Y., Wang, J., Ortiz de Montellano, P. R., and La Mar, G. N. (2006) Solution NMR study of environmental effects on substrate seating in human heme oxygenase: Influence of polypeptide truncation, substrate modification and axial ligand, *J. Inorg. Biochem. 100*, 97−107.
56. Englander, S. W., and Kallenbach, N. R. (1984) Hydrogen exchange and structural dynamics of proteins and nucleic acids, *Q. Rev. Biophys. 16*, 521−655.
57. Sugishima, M., Sakamoto, H., Higashimoto, Y., Noguchi, M., and Fukuyama, K. (2003) Crystal structure of rat heme oxygenase-1 in complex with biliverdin-iron chelate, *J. Biol. Chem. 278*, 32352−32358.
58. Zeng, Y., Deshmukh, R., Caignan, G. A., Bunce, R. A., Rivera, M., and Wilks, A. (2004) Mixed regioselectivity in the Arg-177 mutants of *Corynebacterium diphtheriae* heme oxygenase as a consequence of in-plane heme disorder, *Biochemistry 43*, 5222−5238.
59. Wang, J., Evans, J. P., Ogura, H., La Mar, G. N., and Ortiz de Montellano, P. R. (2006) Alteration of the regiospecificity of human heme oxygenase-1 by unseating of the heme but not disruption of the distal hydrogen bonding network, *Biochemistry 45*, 61−73.
60. Nguyen, B. D., Xia, Z., Yeh, D. C., Vyas, K., Deaguero, H., and La Mar, G. (1999) Solution NMR determination of the anisotropy and orientation of the paramagnetic susceptibility tensor as a function of temperature for metmyoglobin cyanide: Implications for the population of excited electronic states, *J. Am. Chem. Soc. 121*, 208−217.

BI061747Q